

High heating rate effects in sintering: A phase-field study of La-doped alumina

Marco Seiz^{1,*} and Tomohiro Takaki^{1,2,*}

¹Faculty of Mechanical Engineering, Kyoto Institute of Technology,
Matsugasaki, Sakyo-ku, Kyoto 606-8585, Japan

²High-Performance Simulation Research Center, Kyoto Institute of
Technology, Kyoto Institute of Technology, Matsugasaki, Sakyo-ku,
Kyoto 606-8585, Japan

*marco@kit.ac.jp, takaki@kit.ac.jp

June 13, 2025

Abstract

In recent years high heating rate sintering methods have become a hot topic for reasons of energy efficiency and microstructural optimization. This paper aims to shed light on the microstructural evolution these methods induce by means of phase-field modeling and simulations. A particle-based temperature model suited for the sintering process is developed and coupled with a multiphysics phase-field solver. It is shown that the coupled model exhibits many characteristics typical of high heating rate sintering. Furthermore, the occurrence of temperature and microstructural inhomogeneity as well as their interplay is simulatively explored.

Keywords: sintering ; densification ; grain growth ; heating rate ; microstructure ; phase-field ; simulation

1 Introduction

Sintering is a widespread manufacturing technique which turns a green body, a loosely-packed body of little strength, into a denser, stronger version, shrinking the body in the process. It is used commercially and industrially for the production of everyday items such as coffee cups, more technical usages such as crucibles for use in casting and even as part of the solar cell manufacturing process[1]. Key for the latter applications are the materials properties, which depend on the resulting microstructure after the sintering process. The main microstructural factors for e.g. mechanical strength are the remaining porosity and where it is located as well as the grain size. High strength is usually obtained by a perfectly dense body with a small grain size. However, conventional sintering methods expose the body to high temperatures over long times in order to reach a high density. Over this entire time grain growth can take place, worsening the properties. On top of this, heating a furnace for hours is also wasteful in terms of energy usage. With the challenges posed by climate change, improving energy efficiency and potentially also materials properties is an attractive proposition.

In recent years, so-called high heating rate sintering methods[2, 3, 4] have been explored to achieve these goals. As the name implies, the body is heated up rapidly, likely reducing the energy usage. If densification has a higher activation energy than grain growth, then moving quickly over the “low” temperature regime in which primarily grain growth is active will also yield smaller grains at equivalent density. However, due to the high heat input, process control becomes even more important than in conventional sintering: If too much heat is applied overall, grain growth will happen just the same; if too much heat is applied at once, thermal stresses can crack the body. Furthermore, many heating methods heat only the surface of the body, with thermal diffusion then slowly heating the rest. This does not only imply thermal stresses, but also potentially differential densification, which can lead to even higher stresses as well as de-sintering[5].

While experimental trial and error with sophisticated monitoring can yield usable process parameters, this can become expensive in both monetary and temporal cost. An alternative way to optimize the process is to conduct simulations, given that a model approximating the real process exists. In this paper, such a model is proposed for high heating rate sintering based on the “fast firing” process, in which the green body is quickly inserted into a furnace at the target temperature. This model will be probed whether it is suitable to approximate the process as well as to attack a few basic questions about the high heating rate sintering process:

- When does the temperature inhomogeneity become significant?
- When does temperature inhomogeneity lead to microstructural inhomogeneity?
- Does microstructural inhomogeneity persist once it occurs?

Previous modeling and simulation work on high heating rate sintering while spatially resolving both the temperature field and the microstructure is limited to [6, 7]. Teixeira et al. [6] constructed a discrete element method (DEM), combining classical DEM with sintering laws and thermal evolution by considering convection, radiation and conduction. They could show good agreement for the temperature evolution when compared to experimental data. In contrast to a phase-field approach, they could resolve larger volumes and spans of time, but by virtue of method both grain growth and grain deformation are difficult to include (but see [8] for a DEM approach for including grain growth). Yang et al. [7] constructed a non-isothermal phase-field model of selective laser sintering including melting of the grains. The thermal model included conduction, latent heat as well as the laser heat source. They could show the strong localization of heating effects during selective laser sintering and qualitative agreement with experimental observations. The energy functional employed has the problems described by [9] and the lack of advective terms for the microstructural evolution imply a size effect[10, 11], so data relating to densification should be regarded with care. While there are many works simulating the temperature distribution during various kinds of sintering methods on a part scale without resolving the microstructure, resolving both the temperature and microstructure spatially is as-of-yet not well explored territory, which this paper aims to shed light on.

2 Model and implementation

The model description is split into three parts: First, the overall phase-field model for representing and evolving the microstructure is described. Second, the model used to calculate the grain motion is described. Finally, the models used for the temperature evolution are described. Afterwards, some notes on computational and measurement aspects are given and the parameter choices are described in the final subsection.

2.1 Phase-field model

In this work a multi-phase-field (MPF) model based is coupled with a Kim-Kim-Suzuki (KKS) model for the concentration evolution. The geometry of the microstructure is described with the help of phase-fields, which allow for a geometrically unrestricted description of free-boundary problems. At each point in space, a phase-field vector $\vec{\phi}$ describes the local volume fractions of different phases. For solid-state sintering of a pure material, a vapour phase ϕ_V and arbitrary many grain phases ϕ_α are distinguished. Since the number of grains needs to be sufficiently large, storing the entire phase-field vector per cell would require too much memory and computational power. Instead, only the set of non-zero phase-fields along with their phase-indices $\vec{\phi}^i$ is stored, up to a maximum of 8 entries per cell. This is permissible as the non-trivial phase-field values are concentrated in thin regions called the interface. This approach is based on [12, 13].

The n phase-fields are evolved following the approach of [14], in which the sum of pairwise variational derivatives gives the temporal change, combined with a rigid-body advection term:

$$\frac{\partial \phi_i}{\partial t} = - \sum_{j=0}^{n-1} \frac{2L_{ij}(T)}{n} \left(\frac{\delta F}{\delta \phi_i} - \frac{\delta F}{\delta \phi_j} \right) - \nabla \cdot (v_i \phi_i) \quad (1)$$

with the energy functional

$$F = \int_V \sum_{i=0}^{n-1} \sum_{j=i+1}^{n-1} [a(\phi, \nabla \phi, T) + w(\phi, T)] + \phi_i f_i(c_i) dV \quad (2)$$

$$a(\phi, \nabla \phi, T) = - \frac{A_{ij}^2}{2} (T) \nabla \phi_i \nabla \phi_j \quad (3)$$

$$w(\phi, \nabla \phi, T) = W_{ij}(T) \phi_i \phi_j \quad (4)$$

$$f_i(c_i) = \frac{k_i}{2} (c_i - c_i^{eq})^2 \quad (5)$$

describing the energy of the entire domain. The terms a and w describe the equilibrium profile and account for capillary forces, whereas f describes thermodynamic driving forces. The coefficients L_{ij} , A_{ij} and W_{ij} can be related to materials parameters (e.g. surface energy, grain mobility) as described in [13].

In order to decouple the driving force description from the equilibrium conditions, such that the cited relations hold, the concentration evolution is evolved following [15] with an additional advective term:

$$\frac{\partial c}{\partial t} = \nabla \cdot (D(\phi, T)(\phi_s \nabla c_s + \phi_V \nabla c_V) + c \vec{v}(x)) \quad (6)$$

$$D(\phi, T) = \sum_{i=0}^{n-1} D_i \phi_i(T) + g(\phi_v, \phi_s) D_s(T) + \sum_{\alpha=1}^{n-1} \sum_{\beta=\alpha+1}^{n-1} g(\phi_\alpha, \phi_\beta) D_{gb}(T) \quad (7)$$

in which the subscript s refers to the effective solid phase, i.e. $\phi_s = \sum_{\alpha \neq V} \phi_\alpha$. The diffusion coefficient has contributions from bulk diffusion D_i , surface diffusion D_s and grain boundaries D_{gb} , with the indices α, β only going over the grain phases.

2.2 Motion model

The model for the calculation of the grain velocities v_α is based on [10, 16]. The idea is to determine the vacancy absorption rate at a grain boundary, which is geometrically connected to the velocity jump across the grain boundary. The vacancy absorption

rate is formulated as

$$\frac{dn}{dt} = \frac{n - n_{eq}(\mu_{\alpha\beta})}{t_r} \quad (8)$$

i.e. a simple relaxation to an equilibrium value $n_{eq}(\mu_{\alpha\beta})$ which depends on the average capillary pressure $\mu_{\alpha\beta}$ experienced by both particles. The conversion from number density n to molar fraction c (concentration) is computed as $n = \frac{N_A}{V_m} c$ with Avogadro's constant N_A and the molar volume V_m . The average capillary pressure is approximated by the average of the chemical potential on a particle's surface. Following [10], the velocity jump dv across a grain boundary can be written as

$$dv = \frac{dn}{dt} \frac{\Omega}{A} \quad (9)$$

with the atomic volume Ω and the grain boundary area A . Assuming that all velocity jumps $\Delta v_{ij} = v_i - v_j$ should be fulfilled simultaneously, with justification given in [10], one arrives at a system of equations

$$Cv = \Delta v \quad (10)$$

with the contact matrix C describing the connectivity of the grains. This system is typically overdetermined and hence a least-squares solution satisfying conservation of momentum is sought.

Once the particle velocities v have been determined, the velocity field $v(x)$ for the advection of the concentration and vapour phase-field is interpolated in a rigid-body fashion as

$$\vec{v}(x) = \frac{\sum_{\alpha=1}^{n-1} \phi_{\alpha} \vec{v}_{\alpha}}{\sum_{\alpha=1}^{n-1} \phi_{\alpha}} \quad (11)$$

with α only going over non-vapour phase-fields. This yields a velocity field of uniform level within grains, smooth transitions across grain boundaries and abrupt jumps to zero velocity in the vapour.

2.3 Temperature model

With sintering being a thermally activated process, it is of great importance to resolve the spatiotemporal evolution of the temperature. However, since the thermal diffusivity is typically several orders of magnitude larger than the mass diffusivity, resolving both thermal and mass diffusion at the same time can become computationally expensive. Furthermore, for the present work the heating contributions of both convective and radiative heating shall be included, as to model the ‘‘dunk cycle’’ [17] or ‘‘fast firing’’ [18] variant of high heating rate sintering. This would imply solving a fluid-flow problem for the convective part and a radiative heat transfer problem, both of which are highly computationally expensive. In order to avoid this expense, a simplified thermal model on the particle scale is proposed, similar to the discrete element method of [6]. The starting point is the energy balance

$$c_p \frac{\partial T}{\partial t} = -\nabla \cdot (-\kappa \nabla T) + q \quad (12)$$

$$\int_V c_p \frac{\partial T}{\partial t} dV = - \int_A -\kappa \nabla T d\vec{A} + \int_V q dV \quad (13)$$

in which heat diffusion and a heat source q appear, with the second line converting into the weak form and applying the divergence theorem. Suppose now that we discretize the space occupied by all grains into individual volumes V_i according to the extent of

the grains, then we obtain for each grain

$$\int_{V_i} c_{p,i} \frac{\partial T_i}{\partial t} dV = - \sum_j \int_{A_{ij}} -\kappa_{ij} (\nabla T)_{ij} d\vec{A} + \int_{V_i} q_i dV \quad (14)$$

$$(15)$$

which changes the number of unknowns from the grid used to resolve eqs. (1) and (6) to the number of particles in the domain, which is typically far smaller. The index j here goes over all particles to which i is connected, similar to the contact matrix C from the motion model. This procedure is visualized in fig. 1 for a three-particle configuration. There is an implicit no-flux boundary condition on the particle boundaries (blue), as long as these do not intersect with other particles (light gray regions). The light gray regions describe the contact areas A_{ij} which scales the flux between the particles and are equivalent to the GB areas already being determined in the motion model.

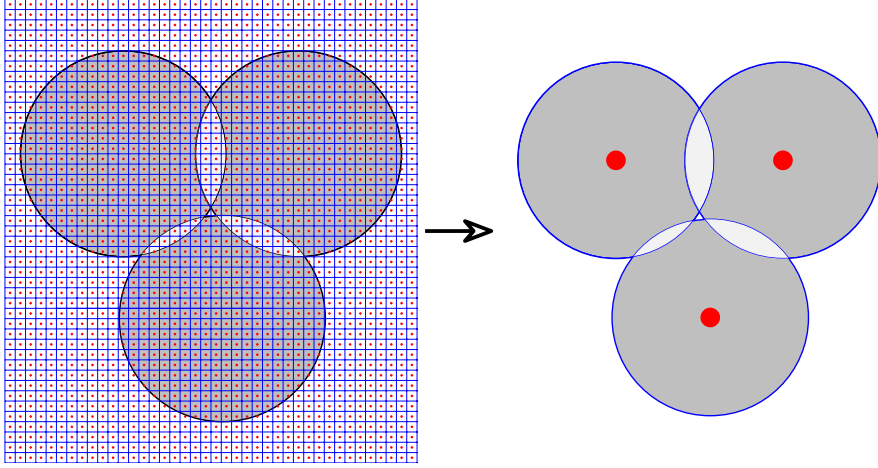


Figure 1: Transformation from grid-wise temperature to particle-wise temperature. Red dots indicate a degree of freedom and blue lines indicate the degree's boundaries.

If we assume further that the particle temperature is homogeneous, we obtain after division by V_i

$$c_{p,i} \frac{\partial T_i}{\partial t} = - \sum_j - \frac{A_{ij} \kappa_{ij}(T)}{V_i} (\nabla T)_{ij} + \int_{V_i} \frac{q_i}{V_i} dV \quad (16)$$

$$= - \sum_j - \frac{A_{ij} \kappa_{ij}}{V_i} \frac{T_j - T_i}{\Delta x_{ij}} + \int_{V_i} \frac{q_i}{V_i} dV \quad (17)$$

which, after time discretization, yields an algebraic system to solve for the new particle temperatures T_i^{n+1} . The thermal conductivity κ_{ij} is calculated as the average of the adjacent particle's temperature-dependent $\kappa(T)$. The heat source q_i ¹ is assumed to only act on the particle surface S based on the furnace temperature T_f and thus is

¹One can also think of the heat source as an imposed flux condition on the free surface of the finite volumes.

written as

$$\int_{V_i} \frac{q_i}{V_i} dV = \frac{S_i q_i}{V_i} \quad (18)$$

$$q_i = q_c + q_r \quad (19)$$

$$q_c = h(T_f - T_i) \quad (20)$$

$$q_r = \epsilon \sigma (T_f^4 - T_i^4) \quad (21)$$

which takes into account heating by convection and radiation, with the convective coefficient h , the emissivity ϵ and the Stefan-Boltzmann constant σ . It is assumed that particles “inside” of the green body do not experience significant heating by these contributions, similar to [6]. Instead of determining the set of “inside” particles a priori however, the particle’s effective surface area S_i is determined during the simulation by a method which assigns zero weight to “inside” particles and non-zero otherwise. This is done by shooting rays from the boundary of the domain until they hit a particle i , at which point S_i is increased. This method naturally accounts for corner and edge effects, as particles located there will have a larger surface area S_i compared to those located on surfaces. The effects of grain growth and grain motion on the heating are also naturally captured with this method.

Given the number of assumptions in the above, a sanity check for the applicability is warranted. For this the Biot number Bi is employed, which relates the contributions due to internal fluxes to the heating at the surface of a body. If $Bi < 0.1$, then the body can be well-approximated as isothermal. This generally holds for the materials and conditions encountered in sintering as shown in the supplementary material.

As particles used in sintering are commonly on the nanometer to low micrometer scale whereas green bodies are in the millimeter and up range, there still exists a scale gap. This is especially relevant for temperature, as by the extensive nature of heat, green bodies of different sizes will heat up differently in the same furnace. Similar to [6], we bridge this scale gap by introducing a separate length scale factor α_L for the temperature evolution, all length-related quantities (distances, areas, volumes) are scaled by α_L or an appropriate power thereof. This effectively scales up the particles and the green body for the temperature evolution, but leaves the microstructure at the smaller scale. One can think of this as an in-situ multiscale model, in which the microstructure at the original scale gives the geometric details for the temperature evolution at the part scale.

Introducing the scale also allows for easy probing of different Biot numbers in order to verify that disregarding internal temperature gradients is justified. For this, an even simpler temperature model is employed, which models the green body as a single large body of volume V and surface area S , which are the sums over the particle-wise values. This lets us write the temperature evolution as

$$c_p \frac{\partial T}{\partial t} = \frac{Sq}{V} \quad (22)$$

with the heating terms and the heat capacity as before. If the temporal evolution between the particle-scale and the green-body scale model lie closely together, then the green body’s internal temperature gradients are negligible. Transitively, if the entire green body’s temperature gradients are negligible, so are the gradients on a particle scale. Given the ratio of particle size to green body size for the present study, the Biot number for the green body is about 30 times that of the particle and thus we can estimate when the particle scale temperature model would under-resolve the temperature field. Also, in order to probe the effects of given heating profiles when the green body can be assumed to be isothermal, the temperature can also be specified as a function of time $T(t)$.

Note that while the model’s time evolution is primarily based on convective and radiative heating terms, the heating rate can be adjusted to match e.g. an external surface temperature measurement curve. This would only involve adding a state-dependent heating term to the surface particles. Thus the model is also applicable to other high heating rate sintering methods as long as the heating is restricted to the surface of the green body. Methods which also heat the interior, e.g. by microwave heating, can in principle also be modeled on a particle basis, as long as the resulting heat input does not impose significant temperature gradients on the sub-particle scale. If it is not, the assumption of isothermal particles could not be held. But given that these methods should naturally penetrate the body, their spatial variance on the particle scale is likely to be small. The heating terms could then be formulated as volume integrals over a power density, given either analytically or via a parallel simulation of the target process.

2.4 Computational notes

The grid-based PDEs eqs. (1) and (6) are solved on a uniform Cartesian grid with finite difference methods. For the non-advective terms, a simple forward-time-centered-space scheme is applied, with divergences being resolved on cell faces as to ensure conservation. The advective terms are discretized with a WENO-Z scheme [19] of order 5 in space and then integrated with a low-storage Runge-Kutta scheme of order 3[20]. By virtue of the advective fluxes being formulated on the cell faces, conservation is also ensured for any advective contribution. The updates are computed on general-purpose graphics processing units (GPU) employing compute kernels. The compute kernels are divided at compile-time into boundary-near and inner kernels, with the former running in advance followed by boundary condition application as to improve parallel scaling. The integrals used in both motion and temperature modeling are largely calculated on the GPUs. The code is parallelized with the Message Passing Interface (MPI) and thus can use any number of GPUs.

When using more than one GPU, the integrals need to be reduced prior to their use: For phase-wise integrals, this is a simple global reduction of size n . For pair-wise integrals, this would require too much memory and communication and thus only existing pairs are integrated and then reduced via one-sided communication. Afterwards, PETSc[21, 22] is employed to build and solve eq. (10) in a least-squares sense and eq. (17) as a nonlinear time integration problem using the first-order backward Euler method. In contrast to [10], in which a global functional shape was assumed to solve eq. (10) with little computational effort, in the present work the full system is solved. This is mainly motivated by the fact that once temperature is no longer homogeneous, a simple linear function cannot represent the velocity profile anymore. Furthermore, since the evolution equations eqs. (1) and (6) are now solved on GPUs, the size of the contact matrix C per worker is increased sufficiently that communication is no longer as much of a bottleneck.

Due to the comparatively small time step and thus small change in state, it is possible to use the integrals of the prior time step as input for eqs. (10) and (17). This allows submitting compute kernels to the GPU and afterwards computing the solution to eqs. (10) and (17) on the central processing unit (CPU), utilizing both the GPU and CPU in parallel. Ideally, it would be possible to step through single iterations during the solution process and check if another kernel can be submitted or boundary conditions need to be applied, i.e. with the multi-stage Runge-Kutta scheme employed for advection. At present however PETSc does not offer such a feature. Thus the work on the CPU can only be hidden completely if it takes less time than the execution of one batch submission of work on the GPU.

The determination of the effective surface area for the particle-wise heating model is similar to a ray tracing problem, though stopping after the first intersection. As the

geometry is only available implicitly from the voxelized phase-field, this is simplified as follows: For each cell, the phase-field index i of the phase-field with the largest phase-field value is determined. This yields a scalar field ranging from 0 to $n - 1$; 0 represents the vapour phase here. If a ray traced from the boundary encounters a non-zero scalar, it stops. The scalar field value at that position serves as the index of the particle surface area S_i to increment. Furthermore, the neighboring values perpendicular to the ray direction are considered to improve the area estimate: If these are of the same index, they are also counted towards the surface area. This would lead to overcounting by a factor of $f_d = 2(d - 1) + 1$, with the dimension d of the simulation domain, on average and thus the resulting sum is divided by this factor. For simple shapes (cubes, spheres) after coarse voxelization this yields the surface area to within about 10% error. By splitting the particle surface area into components per view-direction, it is also possible to introduce directional heating.

Due to the strongly variable memory accesses required for this, the algorithm is not necessarily suited for GPUs. Rather, it is implemented on the CPU and employs a dynamic bounding box to reduce the necessary number of memory accesses. Since the scalar field these calculations are based on only changes quite slowly, this algorithm is executed in the background at least every k steps, including asynchronous MPI communication by the main thread. Early testing showed that the algorithm is finished after less than 10 steps for typical geometries; though since practically the scalar field changes much more slowly, $k = 500$ is chosen. As it is done entirely asynchronously using mainly CPU resources, the algorithm has close to zero impact on the runtime of the simulation.

2.5 Measurement methods

The density ρ is computed by a geometric approach: First, the bounding box of the green body is found via the extremal positions of cells for which $\phi_v < 0.5$. This bounding box generates smaller bounding boxes by moving the edges of the bounding box in increments of $\frac{1}{8}$ of the overall bounding box, resulting in a series of bounding boxes. For each bounding box the integral $\rho = \frac{1}{V_b} \int \phi_s dV$ is computed with the respective bounding box volume V_b and the solid phase-field ϕ_s . As the outermost bounding box includes strong surface effects, it is not used, but rather the first inner bounding box representing about $(\frac{7}{8})^3$ of the green body. By virtue of the initial bounding box determination, if surface diffusion causes the outer particles to temporarily elongate (as e.g. shown by [23] and others), the measured density may temporarily decrease.

The average grain size is based on the particle volumes V_i which are simple volume integrals. The equivalent grain-size based on a sphere is calculated and the volume-weighted average of these is taken to represent the average grain size.

2.6 Parameters

The parameters are generally based on literature data for alumina. Initial tests with grain mobility of pure alumina showed comparatively rapid grain growth, sometimes leaving only a few grains at higher densities which raises questions of statistical accuracy. Thus for the grain mobility the La-doped grain mobility found by [24] is employed. Strictly speaking, the diffusivities should be affected by the La-doping as well; however, due to the lack of temperature dependent data in the literature, the values for pure alumina were employed.

The temperature T dependence of the diffusion coefficients are modeled with Arrhenius functions $D(T) = D_0 \exp(-\frac{E_a}{RT})$ with the parameters D_0 and E_a , as well as the ideal gas constant R . For simplicity, the bulk D_b and vapour D_v diffusion coefficients are taken to be equal. Since the initial compositions of the grains and vapour are in approximate equilibrium, there should be negligible mass transfer between the

phases and hence D_v only plays a minor role. For the conversion of $D_{gb}\delta_{gb}$ to the usual diffusivity units a grain boundary width of $\delta_{gb} = 0.6$ nm[25] is assumed. For the relaxation time t_r , a convergence study using a two particle geometry was conducted at two temperatures. A value for t_r was arbitrarily picked and afterwards decreased until the velocity-time curves showed no more significant differences, i.e. achieved convergence. An Arrhenius function was then calculated based on the results. This ensures that the densification is controlled by diffusion and not the sink efficiency of the grain boundary. The surface mobility M_s is calculated based on the largest diffusion coefficient as to ensure that the surface relaxation is controlled by diffusion and not the phase-field.

The resulting functions are tabulated in Table 1 using 3 significant digits; the full values are available in the supplementary material. The thermodynamic coefficients for eq. (5) are as follows: The equilibrium vapour concentration c_v^{eq} is 0.02, the equilibrium solid concentration c_s^{eq} is 0.98 and the shared prefactor $k_v = k_s$ is 5×10^9 J/m³. The prefactor is chosen high enough such that spontaneous shrinkage due to capillarity [26] is insignificant.

The timestep is calculated based on a maximum eigenvalue estimate of the respective equations eqs. (1) and (6) with a safety factor of 0.2. If this timestep is larger than the time required for the average temperature to change by more than 0.25 K, then the latter time is used for the timestep. This is done in order to account for the vanishingly small mobilities at the simulation start as well as to keep the initial error on the temperature evolution small.

Table 1: Parameters and their sources

parameter	function	source
surface energy γ_s	$2.56 \text{ J/m}^2 - 0.783 \times 10^{-3} \text{ J}/(\text{m}^2\text{K})T$	[27]
GB energy γ_{gb}	$1.91 \text{ J/m}^2 - 0.611 \times 10^{-3} \text{ J}/(\text{m}^2\text{K})T$	[27]
bulk diffusion D_b	$0.32 \text{ m}^2/\text{s} \exp(-\frac{653 \times 10^3 \text{ J/mol}}{RT})$	[28]
vapor diffusion D_v	D_b	-
surface diffusion D_s	$7.2 \text{ m}^2/\text{s} \exp(-\frac{314 \times 10^3 \text{ J/mol}}{RT})$	[29]
GB diffusion D_{gb}	$9.17 \times 10^{10} \text{ m}^2/\text{s} \exp(-\frac{825 \times 10^3 \text{ J/mol}}{RT})$	[28]
GB mobility M_{gb}	$2 \times 10^{-3} \text{ m}^4/(\text{Js}) \exp(-\frac{443 \times 10^3 \text{ J/mol}}{RT})$	[24]
surface mobility M_s	$\frac{1-1}{\gamma_s} \max(D(T))$	-
relaxation time t_r	$1 \times 10^{-20} \text{ s} \exp(\frac{428 \times 10^3 \text{ J/mol}}{RT})$	-
heat capacity c_p	$[1.11 \times 10^3 + 0.14 \frac{T}{K} - 411 \exp(-0.006 \frac{T}{K})] \text{ J/kg}$	[30]
heat conductivity κ	$[5.85 + \frac{15.3 \times 10^3 \text{ K}}{T+516 \text{ K}} \exp(-0.002 \frac{T}{K})] \text{ J}/(\text{Kms})$	[30]
convective coefficient h	$5 \text{ J}/(\text{Km}^2\text{s})$	[6]
emissivity ϵ	0.8	[6]
grid spacing Δx	1 nm	-
interface width W	$6\Delta x$	-

3 Results

For the initial conditions the particle packing also used in [16] is employed. This packing consists of 3431 particles of radius 12 nm, forming a cubic green body with an edge length of about 380 nm. No-flux conditions are applied on all global boundaries. The particles are initialized via planar equilibrium phase-field profiles in the shapes

of spheres, followed by an equilibration to allow for adjustment to curved interfaces and for the initial formation of grain boundaries. For this process the GB mobility is artificially reduced to be insignificant, with both interfacial diffusivities set to zero and $D_b = 1 \times 10^{-12} \text{ m}^2/\text{s}$

The green body's initial state is depicted in fig. 2. For all visualizations of the microstructure, ParaView[31] is used. When presenting the green body without a color map, the maximum non-vapour phase-field ϕ_m is used to produce a contour surface at $\phi_m = 0.6$, which eases differentiation of grains and obtains an etching-like effect at triple and higher order grain junctions. For all plots, matplotlib's[32] Python interface is used.

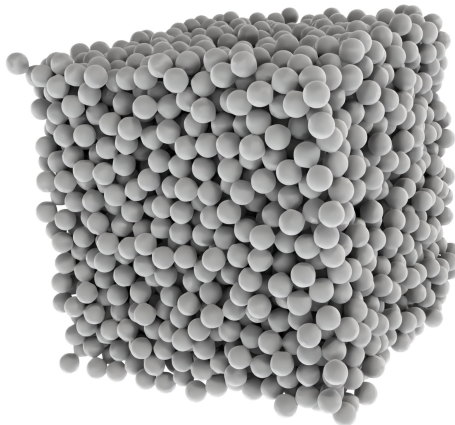


Figure 2: The initial green body configuration is depicted.

The first investigation is concerned with whether effects associated with rapid-heating can be reproduced by employing the simplest temperature model of a given function $T(t)$. There are two qualitative observations we would like to confirm: First, the density observed at a fixed temperature decreases as the heating rate is increased[2]. This is simply due to less time being available for diffusive processes to act. Second, if the activation energy for densification is higher than for grain growth, then at the same density, a lower grain size should be obtained with higher heating rates. This is, again, due to less time being available for grain growth to reduce the driving force for densification before densification itself starts using the driving force. Assuming that the activation energy for grain growth is given via the GB mobility (443 kJ/mol) and that for densification is given via the GB diffusion coefficient (825 kJ/mol), then the present system should show such behaviour.

The second investigation is concerned with inhomogeneous heating effects. Here it is explored when inhomogeneous effects on the microstructure become evident and whether this can be predicted by the Biot number. This includes a verification of the particle-scale model by comparing its predictions with the homogeneous temperature model.

In all cases, the initial particle temperature is $T_i = 300 \text{ K}$, with the end temperature being $T_e = 1800 \text{ K}$, taken on the lower end for sintering temperatures of alumina. If the temperature is specified as a function, this implies a linear ramp up to T_e followed by holding the temperature. Otherwise, the furnace temperature T_f is set to T_e , which implies an evolution towards T_e due to the structure of the heating terms. For simplicity, the end temperature is generally held; realistic heating schedules would include a cooling ramp. Simulations are continued until at least 95% density is reached. Videos of the simulations depicting the entire evolution are deposited with the supplementary material.

3.1 Controlled heating

The first study employs constant heating rates $\dot{T} \in \{50, 125, 250, 500\}$ K/s as a broad sweep across heating rates. Additionally, instantly reaching $T = T_e$ is also considered as to determine whether 500 K/s is practically equivalent to instant heating. The temperature in the domain is thus a simple function of time $T(t)$. The range of heating rates is chosen to be in the range of heating rates achievable by modern high-heating rate experiments[2, 3]. Heating rates as in conventional sintering on the order of 1 K/min are not considered, as their simulations would require an excessive amount of time steps with a forward Euler method. An estimate for the number of time steps dependent on the heating rate is given in the supplementary material; as a simple example, it would take about 33×10^7 steps to reach T_e with a heating rate 0.5 K/s. This number of steps would correspond to about half a year of computation, including queuing times, which is deemed excessive. Future work will consider alternative time integration schemes such that lower heating rates become accessible with acceptable computational effort.

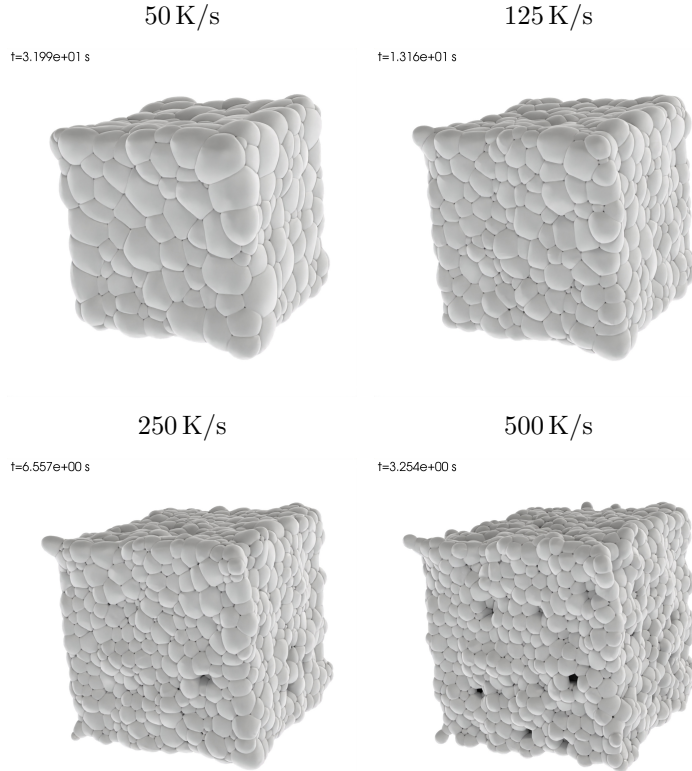
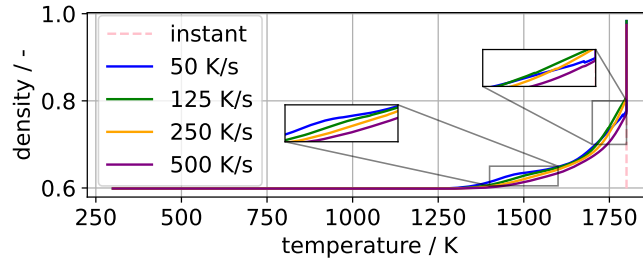


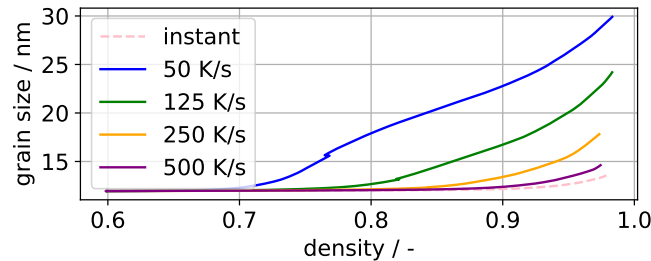
Figure 3: Exemplary microstructures at approximately 90% density are depicted. Note the much larger grains for slower heating rates.

Examples of the resulting microstructures at approximately 90% density are shown in fig. 3. Here one can easily identify much larger grains for simulations with slower heating rates. There also seems to be a trend for the surface to still possess open porosity with faster heating rates; this would be beneficial in atmospheric sintering as to allow gas to escape. These regions visually tend to have the highest number

of surrounding grains and thus their elimination is facilitated by grain growth, as it reduces the coordination number.



(a) temperature-density trajectory



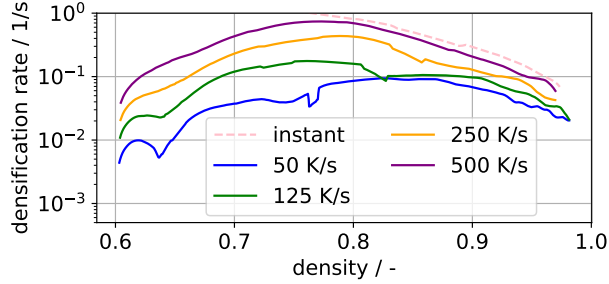
(b) sintering trajectory

Figure 4: Two trajectory types for high-heating rate sintering at a constant heating rate and homogeneous temperature are shown. The qualitative trends of experiments are generally captured, except for the lowest heating rate showing a crossover with higher heating rates at higher density.

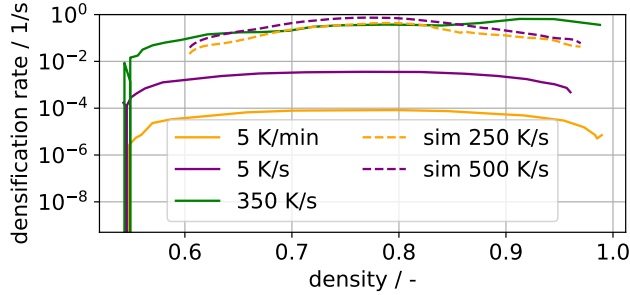
The temperature-density trajectory of the simulations is depicted in fig. 4(a). Initially, the trend for higher heating rates exhibiting a lower density at equivalent temperature is kept, cf. the leftmost inset. The lowest heating rate exhibits a kind of plateau-effect at low densities ($\approx 63\%$), after which it follows a convex trajectory like the other curves. This causes its trajectory to intersect with the two middle heating rates before reaching $T_e = 1800$ K (cf. rightmost inset), contrary to expectations. The remaining trajectories however all show the experimentally observed ordering, i.e. the higher the heating rate, the lower the trajectory is on this plot. While keeping this in mind, consider the sintering trajectories depicted in fig. 4(b): Here the expectations for high-heating rate sintering are fulfilled, with higher heating rates allowing for smaller grain size at the same target density. It can also be observed that with the present materials parameters, even a heating rate of 500 K/s is not exactly comparable to instant heating, even though it would be considered practically instant in experiments. Furthermore, grain growth starts before the final sintering stage is entered ($\approx 90\%$ density). This is due to two reasons: First, nanocrystalline materials tend to show grain growth prior to the final sintering stage[33], both due higher driving forces for grain growth (modeled) and potentially different grain growth mechanisms [34] (not modeled). Second, by virtue of the finite extent of the domain, particles on the outside will experience a different capillary pressure compared to those on the inside. Thus, even though the simulation is started from an almost perfectly uniform size distribution, there is a systematic disturbance which leads to earlier grain growth.

Note that the lowest heating rate does not show significant grain growth during its plateau regime; thus grain growth cannot explain the plateau.

Another compact way to show the effects of high-heating rate sintering is a plot of densification rate over density. This is shown for the present study in fig. 5(a) and below it for the experimental results of [2]. The experiments tend to show a concave curve, with the maximum densification rate occurring around 80% density, with higher heating rates pushing the curve upwards. For the heating rate of 350 K/s it is likely that the temporal resolution of measurements was insufficient to resolve the curve around the maximum densification rate and beyond and thus it shows rather several broad maximum regions. Broad qualitative features are retained in the present simulations, i.e. the concave shape, the maximum at around 80% density and the effect of heating rate. For the experimental heating rate 350 K/s that is bounded by the simulation heating rates, the densification-density trajectory is bounded by the simulation heating rates, as shown by the dashed curves. This suggests that the present model is sufficient to estimate heating schedules for target densities. The earlier plateau is transformed into an early decrease of densification rate here.



(a) simulation results (this work)



(b) experimental results ([2])

Figure 5: Density-densification rate trajectories for the present simulations as well as experimental data from literature. The trajectory is generally concave, showing its maximum around 80% density. The experimental curve for 350 K/s is of the same order-of-magnitude as the simulations which bound this heating rate.

As the averaged properties of the microstructure did not deliver an explanation for the plateau behaviour, the microstructure itself is compared next. A close-up of a planar cut of the solid concentration fields² is shown in fig. 6 for heating rates

²Note that the concentration is not bounded by $[0, 1]$ as the free energy eq. (5) is a parabolic

$\in \{50, 500\}$ K/s at approximately the same density of 63%. The color scale is based on the limits of the simulation with $\dot{T} = 50$ K/s at this point in time. It can easily be seen that the lower heating rate has a much larger accumulation of solid on the grain boundaries than the higher heating rate. This accumulation is caused in the first place by the compressive velocity profile across grain boundaries, which implies some amount of accumulation. Since the absorption dynamics (eq. (8)) depend on the difference of the local concentration and an approximated equilibrium concentration $c_{eq}(\mu_{\alpha\beta})$ of the grains forming the GB, such accumulation will significantly affect the dynamics. Given that $c_{eq}(\mu_{\alpha\beta}) = c_{0,s} + \frac{\mu_s}{k}$ is based on the surface chemical potential $\mu_s \approx \gamma/r$ and with the value of $k = 5 \times 10^9$ J/m³ employed in this work, $c_{eq}(\mu_{\alpha\beta}) - c_0 \leq 0.1$, i.e. significantly below the observed concentration accumulation of up to 1.2 ($c - c_0 = 0.3$). Thus this accumulation leads to a temporary slowdown of densification dynamics, as GBs with this accumulation can contribute de-densifying terms to the system eq. (10); note however that since not all GBs show such an accumulation that the net solution is still densifying. At higher heating rates GB diffusion is already sufficiently activated as to redistribute the accumulation on a similar timescale as it occurs, at equivalent density.

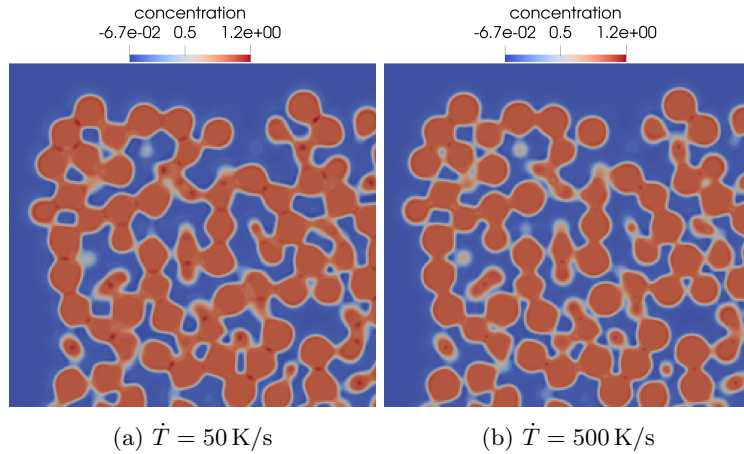


Figure 6: Solid concentration field at about 63% density for two heating rates. The lower heating rate shows larger and longer-lasting accumulation of solid concentration on the grain boundary, causing a plateau in the densification curve.

Since this effect was only observed for a single simulation, with the simulative trends following experimental trends otherwise, the present paper will only list a few possible remedies: The most obvious is one is projecting the velocity field to a divergence-free space, as commonly done in incompressible fluid dynamics. This would involve calculating a divergence and a gradient as well as solving an additional Poisson equation at each step, with the latter likely taking longer than the rest of the solver combined if forward Euler time stepping is employed. Another method could be, given that the gradient of chemical potential is sufficiently smooth in the grain boundary, to direct the advective flux along the gradient of chemical potential in the grain boundary. This method would resolve the accumulation by transporting it quickly along the grain boundary to the sintering neck, similar to the action of GB diffusion at higher heating rates. It would only involve gradient calculations and local interpolations and thus be comparatively cheap. A separate work investigating both approximation.

of these methods is planned.

Sintering models based on solving the incompressible Navier-Stokes equations accounting for microstructural effects such as [35] would typically not exhibit the accumulation effect given the assumption of incompressibility. However, these models have, to the authors' knowledge, only been used for the computation of viscous sintering, which does not involve GBs as necessary sinks for vacancies. Whether these models can be extended to account for vacancy sink activity is another point for future work. Using such kinds of models also requires the use of time integration schemes with less restrictive stability bounds as to compensate for the high computational cost of solving the incompressible Navier-Stokes equations.

3.2 Uncontrolled heating

In this study, the green body ($T = T_i$) is inserted into a pre-heated furnace at $T_f = T_e$, which causes the green body to heat up by convection and radiation. Two models for the temperature are employed and compared herein, the particle-resolving, inhomogeneous model eq. (17) and the homogeneous model eq. (22). Both models are calculated for three different thermal length scale factors $\alpha_L \in \{1 \times 10^3, 5 \times 10^3, 1 \times 10^4\}$, corresponding to initial scaled green body sizes of $L \in \{0.38, 1.9, 3.8\}$ mm respectively. The total Biot number of the green body, estimated at $T = T_f$, is about 0.017, 0.085 and 0.17 respectively. This indicates that one should not see significant differences between the models for $L = 0.38$ mm, but they should start appearing for the larger two green bodies.

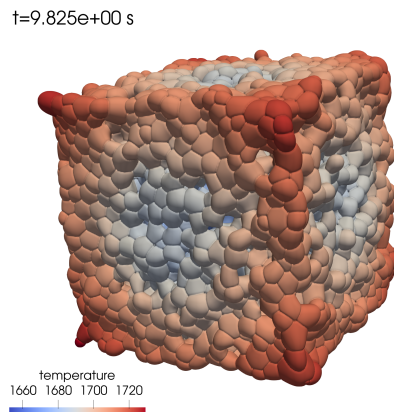


Figure 7: Temperature distribution at 70% density for $L = 3.8$ mm and a particle-wise resolved temperature field. By virtue of the edge effect, corners and edges heat up faster than faces and the interior of the green body is cooler still.

For inhomogeneous heating, a certain spatial profile develops. As an example of this, the temperature distribution is depicted in fig. 7 at about 70% density for $L = 3.8$ mm: The corners and edges of the cubic green body exhibit the highest temperature, with the middle of the faces being cooler, and the inside of the green body even cooler. This is to be expected simply due to edge effects which are naturally captured by the heating model. The temperature distribution is qualitatively similar independent of the green body size, with the main effect of green body size being the temperature difference scale. At this stage the temperature difference between inside and outside is only about 80 K. In the early stages this temperature difference can be up to 1000 K, which would imply significant thermal stresses if they were modeled.

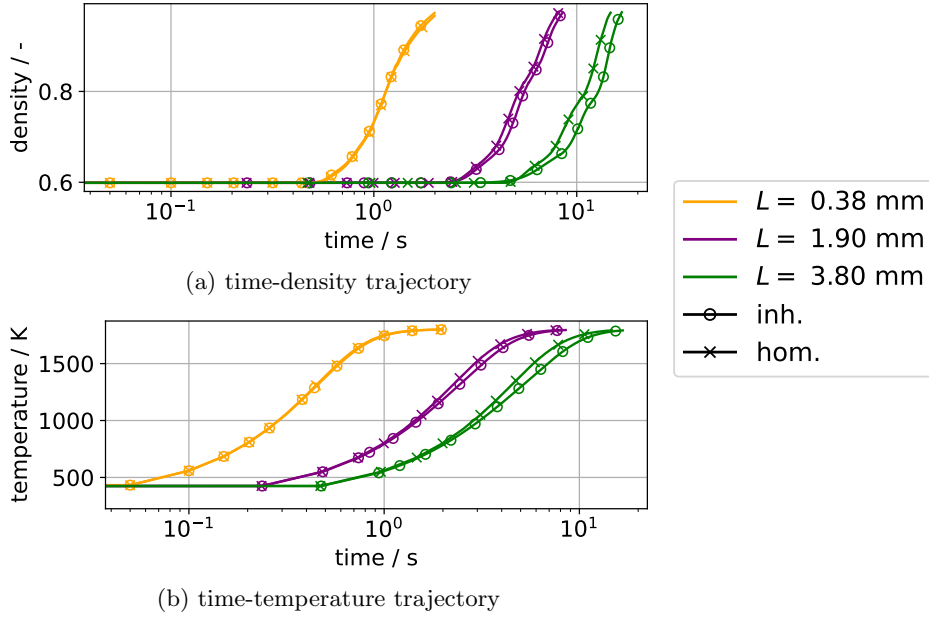


Figure 8: Time and temperature trajectories for uncontrolled heating are depicted. The size of the green body L , and thus the Biot number, gives a good indication of when the inhomogeneity of the temperature starts to affect the evolution, i.e. when the markers of the same color do not match each other.

In fig. 8(a) the density-time trajectories of the simulations are plotted. Here one can observe that indeed $L = 0.38$ mm shows little difference between either model and that once the Biot number is large enough, the microstructural evolution of the green body is affected, with the density-time curves shifting ever wider apart with increasing Biot number. A similar trend is observed in the temperature-time curve depicted in fig. 8(b), with the average temperature differing substantially for higher Biot numbers before closing in on T_f . This also shows the extensive effect of heat: The larger the green body, the longer it will take a furnace at a fixed temperature to heat it to a certain temperature, as the heat input does not scale linearly with the total heat capacity of the green body. Based on these observations, it is confirmed that the Biot number is a good predictor for temperature inhomogeneity for a complex microstructure in a furnace. For the present case we can quantify $\text{Bi} \ll 0.1$ for approximate temperature uniformity as $\text{Bi} \leq 0.017$.

The sintering trajectories of these simulations is shown in fig. 9. As expected, a smaller green body allows for a smaller grain size at the same density due to heating more quickly. However, all curves show a difference between the two heating models, regardless of the Biot number. This can be attributed to inhomogeneity in the temperature leading to microstructural inhomogeneity. Interestingly, the simulations with the largest Biot number and thus inhomogeneity do not show the largest difference in trajectory. In order to explain this, a look at the microstructure is necessary. These are exemplarily shown in fig. 10 at approximately 75% density. First, note that at the smallest Biot number ($L = 0.38$ mm) there is hardly any difference in microstructure. Second, when increasing the Biot number, a change in the microstructure is observable: The surface tends to look more dense via the same mechanism as for high heating rates, i.e. grain growth reducing pore coordination number. Finally, at higher Biot numbers, the inhomogeneous temperature simulations tend to already show grain

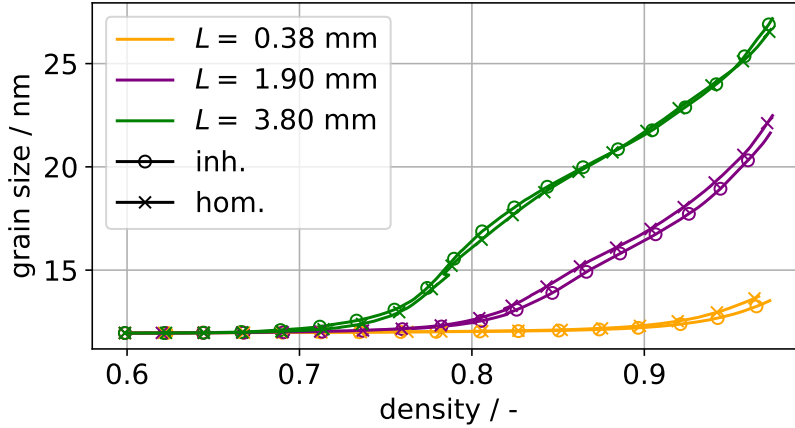


Figure 9: Sintering trajectory for uncontrolled heating. Since smaller green bodies sinter more quickly, they also exhibit lower grain sizes at the same density. The variation in trajectory between the models is not a simple function of the green body size.

growth starting from the corners and edges as these exhibit the highest temperatures. (cf. fig. 7). Thus the lack of divergence *on average* is likely the simple result of the average hiding the difference between the simulations; one could have giant grains on the outside with the same structure inside and obtain a similar average grain size by virtue of the surface to volume ratio.

In order to differentiate microstructures with similar averages but spatial differences, heatmaps of the i -th grain center distance $d_i = \|\vec{p}_i - \vec{c}\|$ and its volume normalized by the current average are depicted in fig. 11: At 75% density one can see a clear difference in the distribution between the temperature models, with a more or less uniform distribution for homogeneous temperature, but a distribution which is slanted to larger grain sizes at larger center distances for inhomogeneous temperature; this is precisely what is observed in fig. 10. However, at larger densities this difference tends to vanish again. This is likely due to the formation and motion of a sintering front[18]: Sufficiently hot grains will activate densification and grain growth on the neighboring GBs, with local densification occurring until these encounter either too cold grains or the driving force has been spent. This process also substantially increases the GB area and thus the heat transfer to colder particles inside, which are then in turn activated to densify and undergo grain growth. As long as the front activates the next inner particles before having densified completely, the front can advance homogeneously through the body, leaving behind a similar structure as in the homogeneous temperature case. The deviation in fig. 11(a) is thus simply due to the front not having advanced yet through the green body.

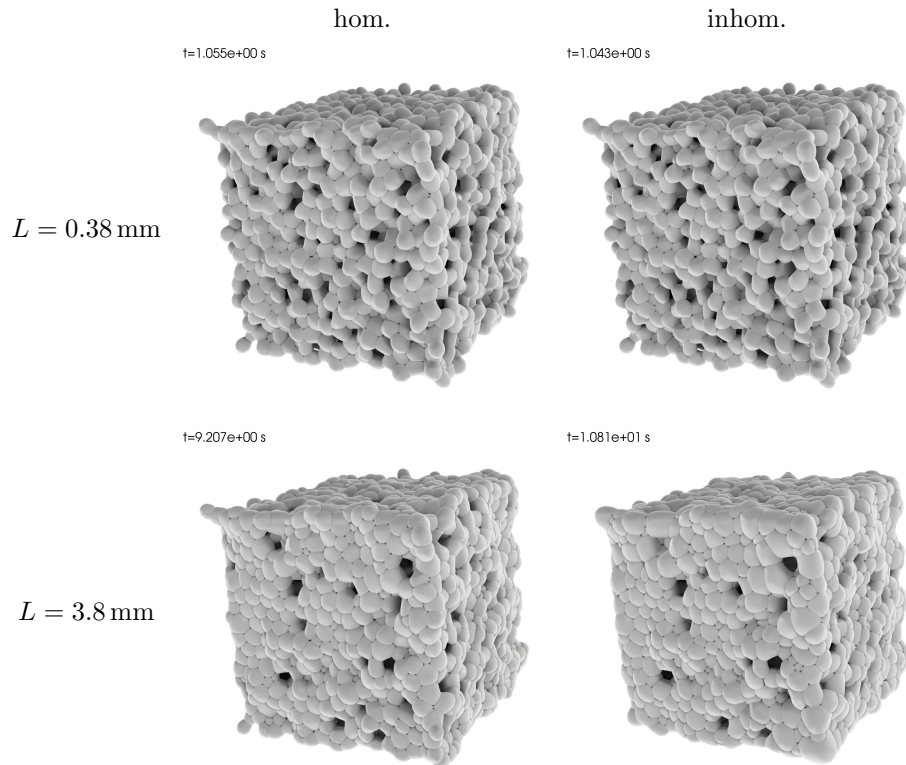


Figure 10: The microstructures at approximately 75% density are shown for various simulations. There is hardly any difference between the temperature models for the smaller green body $L = 0.38$ mm, but a significant one at $L = 3.8$ mm: Both the corners and edges have started grain growth.

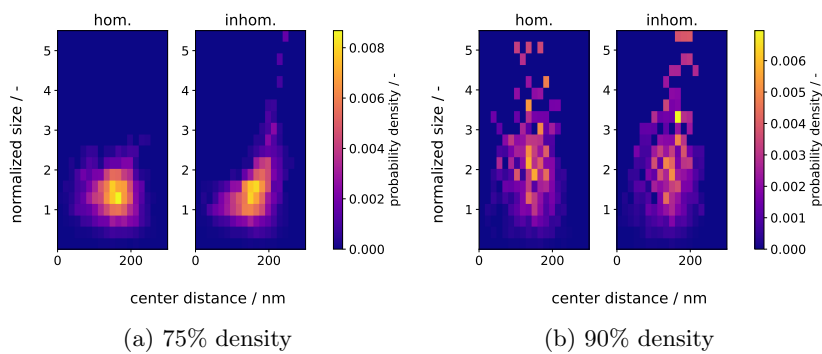


Figure 11: Heatmaps of center distance to normalized grain size for $L = 3.8$ mm for two densities are shown. At lower densities, the microstructural spatial inhomogeneity due to temperature inhomogeneity is visible, but this effect is lost at higher densities due to the sintering front having advanced through the green body.

4 Conclusion

The influence of spatially homogeneous as well as inhomogeneous heating of a green body on its microstructural evolution was explored. For this, a previous phase-field model of sintering was extended to include the temperature dependence of its parameters. Furthermore, a novel and efficient coarse-grained temperature model was developed and implemented to account for the natural multiscale problem presented by sintering. The model bounded a large regime of the density-densification trajectory of one experimental result, suggesting the applicability of the model for real systems.

The questions posed in the introduction can be answered as follows: The conditions when the temperature inhomogeneity in a porous, geometrically complex and evolving green body becomes significant can be predicted well with the Biot number $Bi > 0.017$. Once temperature inhomogeneity becomes significant, microstructural inhomogeneity quickly follows. However, the inhomogeneity need not necessarily persist. If the heat transport inside the body is sufficiently fast, densification on the inside can be activated and match the evolution of the microstructure further outside, i.e. a sintering front emerges. From this one can conclude that for sufficiently small bodies, final homogeneous microstructures can be achieved, even if they temporarily exhibit significant temperature and microstructural inhomogeneity. The conditions for the successful formation of a sintering front depends on the size of the green body, the heating technique, thermal properties as well as factors affecting the densification and grain growth processes. The determination of these conditions would help high heating rate sintering technique development significantly, as it would significantly reduce the effort in determining parameters for the often desired homogeneous microstructure.

Based on these results, it is concluded that the developed model is capable of approximating high-heating rate sintering and predicting the microstructural evolution of experiments, subject to materials parameter adjustments. Future work will include investigation into more efficient time integrators as to access lower heating rates and larger grain sizes with acceptable computational effort. Furthermore, the effect of the compressive velocity profile across grain boundaries will be investigated further and possible avenues for its elimination will be explored, such that the model can also be applied to lower heating rates.

Author contributions

Marco Seiz: Conceptualization, Software, Methodology, Investigation, Data Curation, Validation, Visualization, Writing - original draft, Writing - review & editing.
Tomohiro Takaki: Funding acquisition, Project administration, Resources, Writing - review & editing.

Conflicts of interest or competing interests

The authors declare that there are no conflicts of interest.

Data and code availability

The code required to reproduce the present work cannot be shared publicly. The processed data is available within the supplementary material.

Supplementary Material

The supplementary material of this paper is available at <https://zenodo.org/records/15605646>. It contains interactive and static versions of notebooks reproducing the graphs in the paper, estimates of the Biot number in sintering, the parameters in the employed precision and videos of the simulations.

Acknowledgements

This paper is based on results obtained from a project, JPNP22005, commissioned by the New Energy and Industrial Technology Development Organization (NEDO).

References

- [1] Cori N Bucherl, Karl R Oleson, and Hugh W Hillhouse. Thin film solar cells from sintered nanocrystals. *Current Opinion in Chemical Engineering*, 2(2):168–177, May 2013.
- [2] Dangqiang Wang, Xinzhi Wang, Chongjun Xu, Zhengyi Fu, and Jinyong Zhang. Densification mechanism of the ultra-fast sintering dense alumina. *AIP Advances*, 10(2):025223, February 2020.
- [3] Lukas Porz, Michael Scherer, Daniel Huhn, Luisa-Marie Heine, Simon Britten, Lars Rebohle, Marcel Neubert, Martin Brown, Peter Lascelles, Ross Kitson, Daniel Rettenwander, Lovro Fulanovic, Enrico Bruder, Patrick Breckner, Daniel Isaia, Till Frömling, Jürgen Rödel, and Wolfgang Rheinheimer. Blacklight sintering of ceramics. *Mater. Horiz.*, 9(6):1717–1726, 2022.
- [4] S.Y. Gómez, A.L. Da Silva, D. Gouvêa, R.H.R. Castro, and D. Hotza. Nanocrystalline yttria-doped zirconia sintered by fast firing. *Materials Letters*, 166:196–200, March 2016.
- [5] Fred F. Lange. De-Sintering, A Phenomena Concurrent with Densification within Powder Compacts: A Review. In R.M. German, G.L. Messing, and R.G. Cornwell, editors, *Sintering Technology*. Marcel Dekker Pubs., 1996.
- [6] Mirele Horsth Paiva Teixeira, Vasył Skorych, Rolf Janssen, Sergio Yesid Gómez González, Agenor De Noni Jr, João Batista Rodrigues Neto, Dachamir Hotza, and Maksym Dosta. High heating rate sintering and microstructural evolution assessment using the discrete element method. *Open Ceramics*, 8:100182, December 2021.
- [7] Yangyiwei Yang, Olav Ragnvaldsen, Yang Bai, Min Yi, and Bai-Xiang Xu. 3D non-isothermal phase-field simulation of microstructure evolution during selective laser sintering. *npj Comput Mater*, 5(1):81, August 2019.
- [8] Brayan Paredes-Goyes, David Jauffres, Jean-Michel Missiaen, and Christophe L. Martin. Grain growth in sintering: A discrete element model on large packings. *Acta Materialia*, 218:117182, October 2021.
- [9] Qingcheng Yang, Yongxin Gao, Arkadz Kirshtein, Qiang Zhen, and Chun Liu. An Interfacially Consistent Phase-Field Model for Solid-State Sintering Without Artificial Void Generation. *SSRN Journal*, 2022.
- [10] Marco Seiz, Henrik Hierl, and Britta Nestler. An improved grand-potential phase-field model of solid-state sintering for many particles. *Modelling Simul. Mater. Sci. Eng.*, 31(5):055006, July 2023.

- [11] Marco Seiz, Henrik Hierl, and Britta Nestler. Unravelling densification during sintering by multiscale modelling of grain motion. *J Mater Sci*, 58(35):14051–14071, September 2023.
- [12] Seong Gyoon Kim, Dong Ik Kim, Won Tae Kim, and Yong Bum Park. Computer simulations of two-dimensional and three-dimensional ideal grain growth. *Phys. Rev. E*, 74(6):061605, December 2006.
- [13] T. Takaki, Y. Hisakuni, T. Hirouchi, A. Yamanaka, and Y. Tomita. Multi-phase-field simulations for dynamic recrystallization. *Computational Materials Science*, 45(4):881–888, June 2009.
- [14] I Steinbach and F Pezzolla. A generalized field method for multiphase transformations using interface fields. *Physica D: Nonlinear Phenomena*, 134:385–393, 1999.
- [15] Seong Gyoon Kim, Won Tae Kim, and Toshio Suzuki. Phase-field model for binary alloys. *Physical Review E*, 60(6):7186–7197, December 1999.
- [16] Marco Seiz, Henrik Hierl, Britta Nestler, and Wolfgang Rheinheimer. Revealing process and material parameter effects on densification via phase-field studies. *Sci Rep*, 14(1):5350, March 2024.
- [17] Randall German. *Sintering: From Empirical Observations to Scientific Principles*. 2014.
- [18] Daniel E. García, Dachamir Hotza, and Rolf Janssen. Building a Sintering Front through Fast Firing. *International Journal of Applied Ceramic Technology*, 8(6):1486–1493, November 2011.
- [19] Rafael Borges, Monique Carmona, Bruno Costa, and Wai Sun Don. An improved weighted essentially non-oscillatory scheme for hyperbolic conservation laws. *Journal of Computational Physics*, 227(6):3191–3211, March 2008.
- [20] J.H Williamson. Low-storage Runge-Kutta schemes. *Journal of Computational Physics*, 35(1):48–56, March 1980.
- [21] Satish Balay, William D. Gropp, Lois Curfman McInnes, and Barry F. Smith. Efficient management of parallelism in object oriented numerical software libraries. In E. Arge, A. M. Bruaset, and H. P. Langtangen, editors, *Modern Software Tools in Scientific Computing*, pages 163–202. Birkhäuser Press, 1997.
- [22] Satish Balay, Shrirang Abhyankar, Mark F. Adams, Steven Benson, Jed Brown, Peter Brune, Kris Buschelman, Emil Constantinescu, Lisandro Dalcin, Alp Dener, Victor Eijkhout, Jacob Faibussowitsch, William D. Gropp, V'aclav Hapla, Tobin Isaac, Pierre Jolivet, Dmitry Karpeev, Dinesh Kaushik, Matthew G. Knepley, Fande Kong, Scott Kruger, Dave A. May, Lois Curfman McInnes, Richard Tran Mills, Lawrence Mitchell, Todd Munson, Jose E. Roman, Karl Rupp, Patrick Sanan, Jason Sarich, Barry F. Smith, Hansol Suh, Stefano Zampini, Hong Zhang, Hong Zhang, and Junchao Zhang. PETSc/TAO users manual. Technical Report ANL-21/39 - Revision 3.22, Argonne National Laboratory, 2024.
- [23] Hadrian Djohari, Jorge I. Martínez-Herrera, and Jeffrey J. Derby. Transport mechanisms and densification during sintering: I. Viscous flow versus vacancy diffusion. *Chemical Engineering Science*, 64(17):3799–3809, September 2009.
- [24] Shantanu K. Behera. Kinetics of grain growth in La-doped ultrapure Al₂O₃. *Journal of Alloys and Compounds*, 683:444–449, October 2016.
- [25] S Dillon and M Harmer. Multiple grain boundary transitions in ceramics: A case study of alumina. *Acta Materialia*, 55(15):5247–5254, September 2007.
- [26] Pengtao Yue, Chunfeng Zhou, and James J Feng. Spontaneous shrinkage of drops and mass conservation in phase-field simulations. *Journal of Computational Physics*, 223:1–9, 2007.

- [27] P. Nikolopoulos. Surface, grain-boundary and interfacial energies in Al₂O₃ and Al₂O₃-Sn, Al₂O₃-Co systems. *J Mater Sci*, 20(11):3993–4000, November 1985.
- [28] A.H. Heuer. Oxygen and aluminum diffusion in α -Al₂O₃: How much do we really understand? *Journal of the European Ceramic Society*, 28(7):1495–1507, January 2008.
- [29] Wayne M. Robertson and Roger Chang. The Kinetics of Grain-Boundary Groove Growth on Alumina Surfaces. In W. Wurth Kriegel and Hayne Palmour, editors, *The Role of Grain Boundaries and Surfaces in Ceramics*, pages 49–60. Springer US, Boston, MA, 1966.
- [30] Ronald G. Munro. Evaluated Material Properties for a Sintered alpha-Alumina. *Journal of the American Ceramic Society*, 80(8):1919–1928, August 1997.
- [31] James Ahrens, Berk Geveci, and Charles Law. ParaView: An end-user tool for large data visualization. In *Visualization Handbook*. Elsevier, 2005.
- [32] J. D. Hunter. Matplotlib: A 2D graphics environment. *Computing in Science & Engineering*, 9(3):90–95, 2007.
- [33] I.-Wei Chen and X.-H. Wang. Sintering dense nanocrystalline ceramics without final-stage grain growth. *Nature*, 404(6774):168–171, March 2000.
- [34] C. E. Krill, L. Helfen, D. Michels, H. Natter, A. Fitch, O. Masson, and R. Birringer. Size-Dependent Grain-Growth Kinetics Observed in Nanocrystalline Fe. *Phys. Rev. Lett.*, 86(5):842–845, January 2001.
- [35] Qingcheng Yang and Arkadz Kirshtein. A thermodynamically consistent phase-field-micromechanics model of sintering with coupled diffusion and grain motion. *J Am Ceram Soc.*, 108(3):e20279, March 2025.